Journal of the European Ceramic Society 37 (2017) 3899–3908

Contents lists available at www.sciencedirect.com

Journal of the European Ceramic Society

journal homepage: www.elsevier.com/locate/jeurceramsoc

Development of a processing route for carbon allotrope-based TiC porous nanocomposites

J.P. Ramos [a,b,*], A.M.R. Senos [c], T. Stora [b], C.M. Fernandes [c], P. Bowen [a,**]

[a] Laboratory of Powder Technology, École Polytechnique Fédérale de Lausanne (EPFL), CH-1015 Lausanne, Switzerland
[b] European Organization for Nuclear Research (CERN), CH-1211 Genéve 23, Switzerland
[c] Department of Materials and Ceramics Engineering, Universidade de Aveiro, CICECO, 3810-193 Aveiro, Portugal

ARTICLE INFO

Article history:
Received 27 February 2017
Accepted 7 April 2017
Available online 5 May 2017

Keywords:
Nanocomposites
Titanium carbide
Spallation target
Porous ceramics
High temperature applications

ABSTRACT

Ti-foils are currently used as a spallation target material to produce radioisotopes for physics research at the ISOLDE facility at CERN. However, radioisotope production rates often decrease over time due to material degradation from high operation temperatures. Due to enhanced release rates, porous nanomaterials are being studied as spallation target materials for isotope production. TiC is a material with a very high melting point making it an interesting material to replace the Ti-foils. However, in its nanometric form it sinters readily at high temperatures. To overcome this, a new processing route was developed where TiC was co-milled with graphite, carbon black or multi-wall carbon nanotubes in order to hinder the sintering of TiC. The obtained nanocomposite particle sizes, density, specific surface area and porosity were characterized and compared using ANOVA. All carbon allotropes mixed with the TiC, were able to successfully stabilize the nanometric TiC, hindering its sintering up to 1500 °C for 10 h.

1. Introduction

Titanium carbide (TiC) is a well known FCC interstitial carbide and had its properties studied mainly during the 50's and the 60's [1]. Due to its high melting point of 3067 °C high hardness and strength, good thermal and electrical conductivities, thermal shock resistance, and low evaporation rate it is mainly used as a refractory ceramic. It is used in the aerospace industry (rocket and aircraft materials) and in super-hard and wear-resistant tools (as a cermet and as a coating material) [1,2].

For nuclear applications, TiC has been studied as a coating material [3] or as a reinforcement in carbon for plasma facing materials [4] for future fusion plants. TiC has also been subject to numerous irradiation studies as a potential material for nuclear fuel coatings in fission power plants [5]. In the past, at the ISOLDE (Isotope Separator OnLine DEvice) facility at CERN [6], TiC was studied as a potential spallation target material for production of radioactive ion beams, but the outcome was unsatisfactory due to slow isotope release rates [7,8].

ISOLDE relies on the on-line isotope separation method (Isotope Separator OnLine, ISOL) [6] to produce radioactive ion beams for nuclear, atomic, solid state and bio-physics studies. In this method, a target material kept at high temperatures in vacuum, is irradiated with energetic particles which will induce nuclear reactions in the material, producing isotopes that come at rest in the target. These isotopes have then to diffuse out of the bulk material to the surface where they evaporate and diffuse through the material porosity, defined as effusion. They then effuse through a transfer line into an ion source. The ion source finally transforms the released neutral isotopes into ions and shape a beam for physics experiments [9].

The target materials used for ISOL vary from liquids (low melting point metals or salts), solids in powder, pellet or fiber form (carbides or oxides) or metallic foils [10]. The materials should be as pure as possible, since impurities can produce unwanted isotope contaminants, either through nuclear reactions or vaporization as radiologically stable contaminants. High target material operation temperatures are needed to accelerate the diffusion and effusion processes while being limited by the material melting point, vapor pressure and sintering rates. A highly porous microstructure with the smallest particle size is desired, to reduce the diffusion distances but it has to be stable at the highest operation temperature. Reducing the particle size of the target material either to submicrometric [11,12] or nanometric [10,12–14] has shown in the past

* Corresponding author at: European Organization for Nuclear Research (CERN), CH-1211 Genéve 23, Switzerland.
** Corresponding author.
E-mail addresses: joao.pedro.ramos@cern.ch (J.P. Ramos), paul.bowen@epfl.ch (P. Bowen).
URL: http://www.joaopedroramos.com (J.P. Ramos).

http://dx.doi.org/10.1016/j.jeurceramsoc.2017.04.016

enhanced isotope release and, consequently, higher beam intensities for short lived species.

Historically, micrometric TiC (1–50 μm) was discarded as a target material due to slow release of isotopes even at 2300 °C [7,8]. Micrometric SiC (1–50 μm) was discarded as well for the same reasons [8], and in recent developments, by reducing SiC particle size to the sub-micron level (0.6 μm) the release of isotopes was shown to be improved [11,12]. We propose to use the same methodology for TiC, reducing its particle size down to the submicron or nanometric level. Additionally, particle size stabilization mechanisms can be employed leading to higher operation temperatures. Such mechanisms can be achieved by doping TiC or by introducing a second highly-refractory inert phase, such as carbon, to reduce the coordination number of TiC particles and hinder sintering.

The sintering driving force is provided by the decrease of the free energy of the system which depends on the total free surface and particle radius and curvature. As such, the sintering kinetics of nanomaterials are enhanced when compared to conventional materials, because of their intrinsic high surface areas. While conventional powders are expected to sinter at about 0.5–0.8 T_m (T_m being the material melting point), in nanomaterials this can happen at 0.2–0.4 T_m [15]. In the literature, TiC powders with 140–170 nm primary particle size, reached 91% density at 1627 °C while 5 μm TiC powders needed 2797 °C to reach the same density [16]. Furthermore, nanopowders are often found in an agglomerated form, having a bimodal pore size distribution: small intra-agglomerate and large inter-agglomerate pores [17]. While the small pores from the intra-agglomerate porosity are easily eliminated during sintering, the large inter-agglomerate pores require significantly higher temperatures. The sintering temperature of nanomaterials often scales up with the agglomerate size, rather than with the primary particle size [15]. Since ISOL targets operate at high temperatures and nanometric materials tend to sinter readily, a solution which allows for high diffusion/effusion and at the same time low sinterability has to be found [14,13].

Dual-phase sintering or constrained sintering is used in ceramics to prevent grain growth by having two homogeneously mixed and interpenetrating phases which have limited or no solid solubility with each other [18,19]. There are examples in the literature where grain growth and densification was successfully hindered in ZnO–SiC [20] systems, Al_2O_3–ZrO_2 [19] and Al_2O_3–Cu [21]. For the TiC-C system a study done by B. Manley et al. [22] shows that additions up to 14 at.% (3.2 wt.%) of C, hinder the sintering of submicrometric TiC by reducing the relative volume changes by more than a factor of 2. Furthermore, in SiC, it has been shown that the addition of very small quantities of carbon (up to 3 wt.%) promote sintering (with 0.5 wt.% B) while further additions, studied up to 16 wt.%, successfully hinder its grain growth [23].

TiC-C (nano)composites can be found in the literature in a wide range of sizes (4 nm to tens of micron), shapes (fibers or particles) and different TiC volumes (5 vol.% to almost 100% TiC) [4,24–35]. A considerable amount of the TiC-C studies are found for fiber shape where normally the carbon is a by-product from the TiO_2 carbothermal reduction with C. Such fibers are used in reinforced polymers with 300 nm fiber diameter [24], semiconductor films with tens of micron diameter fiber [25], filtration membranes, 120 nm mesoporous fibers with 19 nm TiC crystallites [26], solar cells with 200–400 nm fiber diameter with 20 nm TiC crystallite size, 70 wt.% TiC [27] and for supercapacitors with 280 nm diameter fibers, TiC crystallite size 20–50 nm, 40 wt.% TiC [28]. In the rest of the studies found, TiC-C composites include application in electrodes and catalysis (4 nm TiC, 30 wt.% Ti as membranes [29] or 35 nm TiC-C core–shell particles [30]), fuel cells (25–75 wt.% of micrometric TiC in C as coating [31]), as high temperature structural material (tens of micron TiC with 2–40% of C, 15% porous to fully dense [32–34] or with 100 nm TiC crystallite size, 30% porous with 9/1 – Ti/C molar ratio [35]) and for nuclear applications (5 vol.% ≈100 nm TiC inclusions in graphite [4]).

Although, TiC-C composites already exist in the literature, as seen above, their processing is either too complex or not suitable for the application described here. Moreover, the structure required is one which should be stable at high temperatures (at least 1500 °C) while keeping nanometric TiC, which was not found in the literature. Additionally, the simplest processing route should be used to reduce and control the possible sources of contamination to the target material. Since the titanium is the element of interest (selected due to the high isotope production cross-sections), one wants the highest concentration as possible while keeping acceptable levels of open porosity. Also, the processing route must be easy to scale up, since TiC targets are expected to have up to 100 g. As a result, in order to stabilize nanometric TiC with size less than 100 nm, a new processing route is developed here where different ratios of carbon allotropes, graphite, carbon black and carbon nanotubes, are added to the TiC. The TiC-C composites obtained were characterized before and after heat treatments in order to assess the degree of stabilization of nanometric TiC.

2. Materials and methods

2.1. Materials

Commercially available nanometric TiC powder was acquired from *Goodfellow*, 99.9% pure, with nominal particle sizes between 80 and 130 nm (Ref. LS396999/1). The carbon allotropes used were: graphite (*Alfa Aesar*, Ref. 40798, 325 mesh – <44 μm), carbon black (*Orion Engineered Carbons*, *Printex A Pulver*, 40 $m^2 g^{-1}$ – 40 nm primary particle size) and multi-wall carbon nanotubes, MWCNT, (*Nanocyl*, Ref. NC3100, >95% purity, 10 nm diameter, 1.5 μm length). The mixtures were done in isopropanol, IPA, (from *Reactolab SA*, Ref. 99295, 99% pure) using polyvinylpyrrolidone, PVP, (*Fluka*, K-30 mol wt 40k) as a dispersant for the TiC and the allotropic carbon materials [36]. The characteristics of the raw materials can be found in Table 1 and scanning electron microscope microscopy (SEM) microstructures in Fig. 1.

2.2. Methods

2.2.1. Processing

The TiC-C composites were co-milled using an attrition mill (*Union Process, 01HD*) at 800 rpm in a small volume grinding bowl (70 ml) using 1.5 mm yttrium-stabilized-zirconia (YSZ) milling balls. The milling suspension was added to the grinding bowl with 2.6 vol.% of solids in IPA containing 0.5 wt.% PVP and 130 g of YSZ balls were added to fill the grinding bowl up to 90%. Preliminary studies on the milling of the raw materials were done interrupting the milling process at defined times to take small samples. After these studies and optimizations, 2 h was defined as milling time to produce the TiC-C composites. In the case of the MWCNT, the bulk density (see Table 1) was used to calculate the MWCNT solid volume, because they dominate the mixing behavior. The carbon volumes tested were 25, 50 and 75 vol.%.

In the case of the MWCNT composites an additional composite was produced where the MWCNT were not co-milled with the TiC. This composite, was produced by milling the TiC for 2 h separately and later mixed with MWCNT which were treated by ultrasonication for 15 min beforehand. The TiC milled suspension was added to the MWCNT suspension and sonicated for a further 30 min.

After the milling/mixing process, the suspensions were dried using a rotary evaporator (*Buchi Rotovapor R-114*), at 80 °C in vacuum with constant agitation to avoid segregation of the TiC from the carbon. The obtained powder was deagglomerated manually

Table 1
Characteristics of the raw materials used in this study, where SSA is the specific surface area, P_S is the median pore size, $v_{P,BJH}$ is the pore volume (both determined by nitrogen adsorption–desorption using the BJH model) and $D_{v,50}$ is the average particle size.

Characteristic	TiC	Graphite	Carbon Black	MWCNT
Density ($g\,cm^{-3}$)	4.93 [37]	2.16 [37]	1.85[a]	2.16[b] (0.15[a] - bulk)
Dimensions	80–120 nm[a]	<44 μm[a]	≈40 nm[a]	9.5 nm × 1.5 μm[a]
SSA ($m^2\,g^{-1}$)	25.1	2.1	36.9	293.1
G_{BET} - k_S[c]	48 nm - 6	5.3 μm - 24	88 nm - 6	-
P_S (nm)	41	62	70	38
$v_{P,BJH}$ ($cm^3\,g^{-1}$)	0.07	0.02	0.43	2.70
$D_{v,50}$ (μm)	1.70	33.17	0.46	42.79
A_F[d]	35.4	6.3	5.2	n.a.

[a] Given by supplier.
[b] Graphite density assumed for MWCNT theoretical density.
[c] $G_{BET} = k_S/(SSA * \rho_t)$, where G_{BET} is the particle size and k_S is a parameter depending on the shape; $k_S = 6$ – for spheres; $k_S = 24$ – for 1:10 flakes [38].
[d] $A_F = D_{v,50}/G_{BET}$ and represents the agglomeration factor [38].

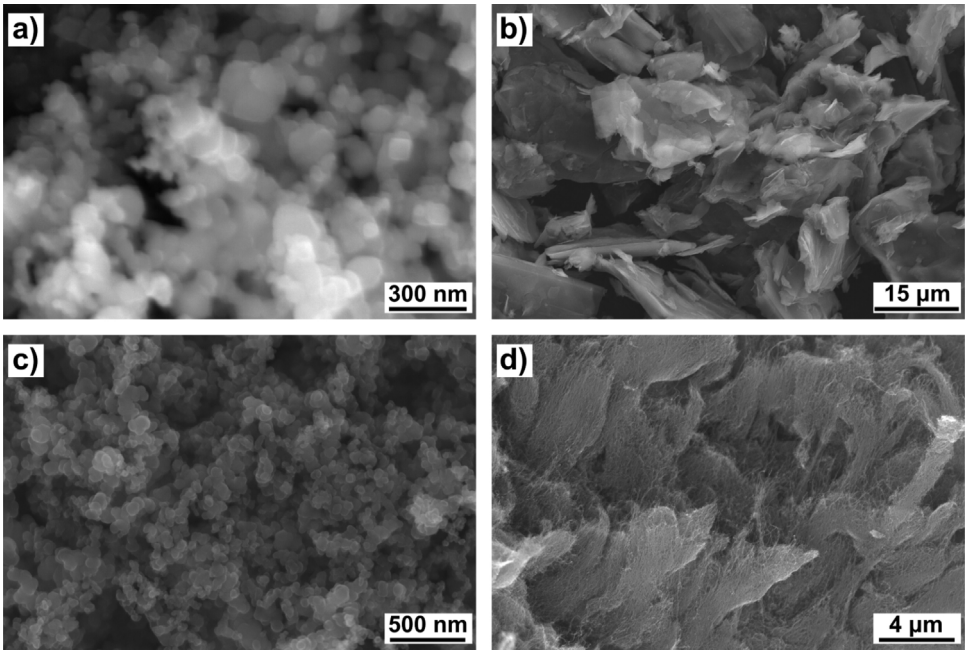

Fig. 1. SEM microstructures of the raw materials used in this study: TiC (a), graphite (b), carbon black (c) and MWCNT (d).

using an agate mortar and pestle, and pressed into 12 mm cylindrical compacts with 1–2 mm thickness, in a hydraulic press at 62 Mpa.

In order to remove the PVP, the powder compacts were pre-heat treated under a flowing argon atmosphere at 450 °C for 3 h (3 °C min^{-1}, heating and cooling) in a quartz tube which was inserted in an horizontal alumina *Heraeus* oven [36]. The samples were then heat treated at 1500 °C in vacuum with holding times of 2 and 10 h with 8 °C min^{-1} heating/cooling ramps. The oven used was a *Carbolite STF 15/450* horizontal alumina tube oven, adapted with in-house made flanges to allow vacuum, which was connected to an *Agilent TPS-mobile TV301* pumping station. Overall, the pressure at 1500 °C reached was around 10^{-3}–10^{-4} Pa. To protect the samples from oxidation and minimize carbon losses (due to residual presence of oxygen), a specially built double layer graphite crucible was designed to introduce the samples (see Fig. A.1.2 in supplementary material).

2.2.2. Characterizations and data handling

The particle size distributions (PSD) and median volume diameter ($D_{v,50}$) during the milling tests, were measured using laser scattering in a *Malvern Mastersizer S*. Before the measurements, the suspensions were ultrasonicated for 15 min. For the laser scattering PSD measurements, the refractive indexes used were 1.38 for IPA [37], 3.05+2.67*i* for TiC [39], 1.84+0.46*i* for carbon black [40], 2.13+1.11*i* for graphite [40] which was also used for MWCNT. The cylindrical powder compacts were measured and weighed in all steps to check for geometrical density (ρ) changes ($\Delta\rho/\rho_0$) and mass losses. Nitrogen adsorption–desorption isotherms were done in a *Quantachrome eNOVA2200*, using the BET (Brunauer–Emmett–Teller) model [41] for specific surface area (SSA) and the BJH (Barrett–Joyner–Halenda) model [42] to determine the pore size distributions and pore volumes ($v_{P,BJH}$). This approach is limited to pores < 200 nm and were evaluated from the desorption branch of the isotherm. The pores were assumed to have a cylindrical shape and the average median volume diameter ($D_{Pv,50}$ or simply pore size, P_S) was determined from the cumulative size distribution obtained from the BJH model. The sample microstructures were obtained using an in-lens detector on a *Carl Zeiss SMT Σigma* SEM. In selected samples the particle size was measured directly from the SEM images (G_{SEM}), measuring 400 particles per sample using *ImageJ* v1.50 [43]. The samples were also studied by dilatometry in a homemade vertical graphite dilatometer, that could reach 1500 °C and was equipped with an LVDT sensor (linear variable differential transformer) to measure sample linear variation or shrinkage ($\Delta l/l_0$) with temperature. The oven was

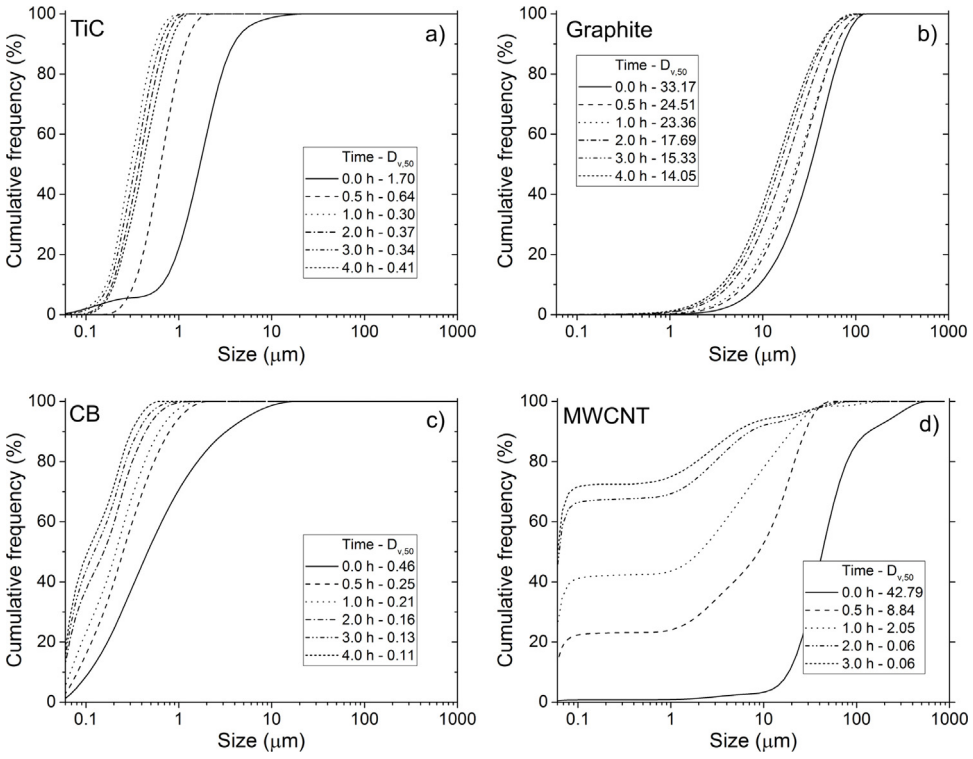

Fig. 2. Particle size distributions for different milling times and respective $D_{v,50}$ values in μm for (a) TiC, (b) graphite, (c) carbon black (CB) and (d) MWCNT.

connected to a primary oil rotary vacuum pump that could reach $1–10^{-1}$ Pa. The heating rate was 8 °C min^{-1}.

Since all composites have different initial characteristics, only a comparison in terms of relative evolution is possible. $\Delta\rho/\rho_0$, the pore size variation below 200 nm ($\Delta P_S/P_{S,0}$) and SSA (S) variation ($\Delta S/S_0$) before and after the 2 and 10 h thermal treatments at 1500 °C were calculated in the following way:

$$\Delta X/X_0 = (X - X_0)/X_0 \quad (1)$$

where X stands for either ρ, S or P_S, the measured value after heat treatment and X_0 for ρ_0, S_0 or $P_{S,0}$, the same characteristic before the heat treatment.

The experiments were organized in a statistical design with 2 samples for each thermal treatment (1500 °C – 2 and 10 h) for each composite. A schematic with the statistical design can be found in Fig. A.1.1 on supplementary materials. The results were analysed by factorial ANOVA, statistical analysis of variance [44] in order to study the evolution of the described characteristics with the carbon allotrope and volume ratio added to the TiC.

Samples were named X{carbon} where X is vol.% of carbon added and {carbon} is the carbon allotrope added: CB, Gr, CNT and TiCm standing for carbon black, graphite, MWCNT and TiC milled without carbon, respectively. So, for example, 50Gr corresponds to the 50 vol.% graphite mixed with TiC. For the case where the MWCNT were not co-milled with the TiC this sample will have a {Carbon} name as CNTb.

3. Results and discussion

The carbon allotropes were chosen in order to have as different a size and morphology as possible to assess the TiC sinterability when mixed with the allotropes. The SEM images in Fig. 1 show nanometric spheres for TiC and CB, micrometric flakes for graphite and tens of nanometer thick tubes/rods for MWCNT. The effective primary particle sizes, G_{BET} (Table 1) were, 48 nm for TiC, 88 nm for carbon black and 5.3 μm for graphite.

In total, during this study, 11 materials were produced and heat treated at 1500 °C for 2 and 10 h: TiC, TiCm, 25Gr, 50Gr, 25CB, 50CB, 75CB, 25CNT, 50CNT, 75CNT, 75CNTb. Only 5 of the produced materials were selected to be discussed in this article: TiC, TiCm, 50Gr, 50CB and 75CNTb (and partially 75CNT). The results for the other composites, which do not add value to the discussion, can be found in supplementary material A.1.2.

In the following subsections the milling optimization will be firstly discussed, as well as its influence on the agglomerate size of TiC, which affects its sinterability. Then, the sintering behavior of TiC at 1500 °C will be discussed to serve as a comparison for the nanocomposites. Finally, the influence of each carbon allotrope (Graphite, CB and MWCNT) on the sintering of TiC will be discussed independently and compared with the other composites. This will be done following the evolution of the composite characteristics, ρ, SSA and P_S as well as microstructure morphology together with dilatometry. Relative density (ρ_r) and porosity were also used to characterize the nanocomposites. The porosity ($P_r = 1 - \rho_r$) was divided in porosity below 200 nm ($P_{r,<200\,nm}$), determined from $v_{P,BJH}$, and porosity above 200 nm ($P_{r,>200\,nm}$), determined from the later and the relative density. The calculation of ρ_r, $P_{r,<200\,nm}$, $P_{r,>200\,nm}$ can be found in supplementary material A.1.1.

3.1. Milling influence on the raw materials

The lowest possible degree of agglomeration is desired for the synthesis of the nanocomposites to have homogeneous mixtures. Laser scattering is able to detect agglomerates (assemblies of primary particles) giving an agglomerate size distribution, represented by $D_{v,50}$. G_{BET} is more indicative of primary particle size since it is not very dependent on the degree of agglomeration as it is determined from the total SSA. The ratio of these two parameters, $D_{v,50}$ and G_{BET}, can be used to determine the agglomeration factor, A_F, as shown in Table 1.

As seen in Fig. 1, all powders are in an agglomerated form. While both CB and TiC are heavily agglomerated as seen in the SEM fig-

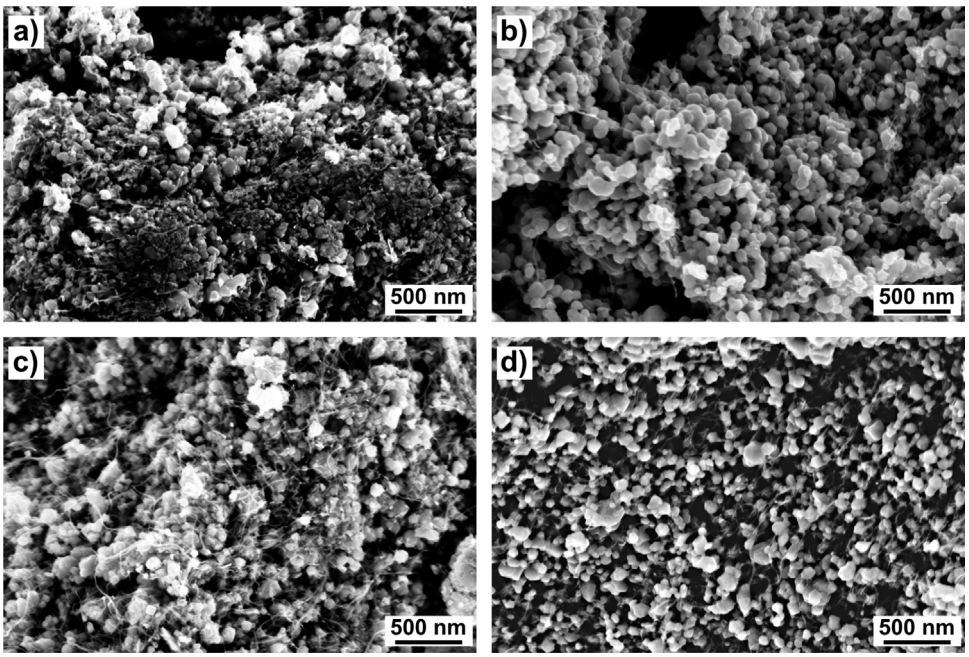

Fig. 3. SEM microstructures of 75CNT as-produced (a) heat treated at 1500 °C for 10 h (b) and of 75CNTb (MWCNT not milled) as-produced (c) and heat treated at 1500 °C for 10 h (d). For the latter, G_{SEM} is 62 ± 26 nm.

ures (Fig. 1a and c respectively) their A_F is quite different, 6.3 and 35.4 respectively as seen in Table 1. This is likely related with the nature of those agglomerates, where in TiC case they could be more difficult to break during the sample preparation for laser scattering which uses agitation and sonication.

The particle size distribution was used to follow the evolution of milling of the raw materials. The powders were individually milled up to 4 h and particle size distributions were taken at 0, 0.5, 1, 2, 3 and 4 h of milling, as shown in Fig. 2.

During attrition milling, the titanium carbide $D_{v,50}$ changes from 1.70 μm to 300 nm in the first hour of milling, stabilizing in the 300–400 nm range for longer milling times, as seen in Fig. 2a. For graphite, $D_{v,50}$ keeps reducing for longer milling times, from 33.17 μm to 14.05 μm for 4 h (Fig. 2b). In the case of CB, the milling is very efficient in destroying the CB agglomerates, where, after 4 h of milling, the $D_{v,50}$ (110 nm in Fig. 2c) almost matches the primary particle size value in Table 1 – G_{BET}=88 nm.

In the case of TiC milled for 2 h (TiCm), the SSA was determined to be 29.4 $m^2\ g^{-1}$, from which the G_{BET} obtained is 41 nm. This gives an A_F for TiCm of 9.0 (from A_F of 35.4) showing a significant reduction of the TiC agglomeration through attrition milling. Since little influence on TiC $D_{v,50}$ was seen at longer milling times, these milling settings were chosen for the nanocomposites production.

There is a very significant impact of the milling on the MWCNT where, in Fig. 2d, the $D_{v,50}$ is changing from 42.79 μm (an highly agglomerated state – as seen by SEM in Fig. 1d) to 0.06 μm only after 2 h of milling. At 2 h of milling of MWCNT, the cumulative size distribution shows that around 50% of the particles is below 50 nm which is below the detection limit of the equipment. Although this technique is not ideal to measure the MWCNT, due to their shape and size, the particle size distributions in Fig. 2d seem to indicate that the MWCNT are being destroyed ("chopped") during the milling process, as has been seen in other studies [45].

Additionally, when co-milling MWCNT with TiC (75CNT) for 2 h, the MWCNT are obviously being destroyed since they are barely visible before and after heat treatment at 1500 °C for 10 h, in the SEM microstructures of Fig. 3a and b, respectively. In order to overcome this, another mixing method for the TiC-MWCNT composite was attempted (hereinafter 75CNTb): mixing the 2 h milled TiC suspension with a MWCNT suspension previously sonicated. The resulting SEM microstructures before and after heat treatment (Fig. 3c and d), clearly show the presence of MWCNT.[1] The MWCNT milling ("chopping") has a detrimental effect on the TiC sintering hindering, as can be seen from the heat treated 75CNT and 75CNTb composites (Fig. 3b and d, respectively), where the latter has smaller particle sizes. Thus, only 75CNTb nanocomposites were chosen for further discussion in this article.

A contamination of 3–6% of ZrO_2, determined by XRPD (X-ray powder diffraction), was found in all the as-produced nanocomposites which comes from the wear of the milling media due to the hard nature of TiC. After the thermal treatments at 1500 °C the ZrO_2 was reduced to ZrC, as expected due in the presence of carbon.[2] This reduction is the cause of the somewhat high mass losses – 11,12 and 13% respectively for graphite, CB and MWCNT nanocomposites (Table 2), obtained after heat treatments when comparing to TiC (≈6%). This phenomenom and its effect on the nanocomposites are discussed in more detail in another publication [46].

3.2. Nanocomposites sintering behaviour

In order to discuss the composites sintering and respective porosity evolution, a simple phenomenological 4 stage model is proposed and illustrated in the schematic of Fig. 4:

1. as known for nanomaterials, sintering starts predominantly within the agglomerates, due to the high free energy and particle coordination number. The sintering happens through neck formation, bringing large $\Delta S/S_0$ and small changes to ρ_r (coalescence – likely dominated by the surface diffusion sintering mechanism) [15,17,47,48];

[1] More information on the properties of 75CNT can be seen in Figs. A.1.8 and A.1.4 and Table A.1.1 on supplementary material A.1 and can be compared with 75CNTb presented throughout this article.

[2] Refer to X-ray powder diffractogram in Fig. A.1.3 in the supplementary materials A.1.2.

Table 2
Density (ρ), SSA, median pore size (P_S), BJH pore volumes ($v_{P,BJH}$), SEM particle sizes determined with *ImageJ* (G_{SEM}) and mass losses ($\Delta m/m_0$) of TiC, TiCm, 50Gr, 50CB and 75CNTb as-produced and after heat treatments at 1500 °C for 2 and 10 h.

		TiC	TiCm	50Gr	50CB	75CNTb
ρ (g cm^{-3})	As-produced	2.37	2.27	1.87	1.60	1.41
	1500 °C – 2 h	3.19	2.44	1.89	1.69	1.65
	1500 °C – 10 h	3.61	2.64	1.81	1.70	1.79
SSA (m^2 g^{-1})	As-produced	25.1	29.4	32.6	37.5	49.8
	1500 °C – 2 h	1.5	3.2	13.1	21.2	27.0
	1500 °C – 10 h	0.5	2.1	11.9	21.1	23.6
P_S (nm)	As-produced	41	27	27	33	27
	1500 °C – 2 h	35	39	44	40	27
	1500 °C – 10 h	11	27	34	37	28
$v_{P,BJH}$ (cm^3 g^{-1})	As-produced	0.07	0.16	0.17	0.27	0.30
	1500 °C – 2 h	0.01	0.01	0.10	0.20	0.21
	1500 °C – 10 h	0.00	0.01	0.05	0.16	0.21
$\Delta m/m_0$ (%)	1500 °C – 2 h	6.2	6.6	9.4	10.9	10.6
	1500 °C – 10 h	6.9	7.2	10.5	11.3	12.8
G_{SEM} (nm)	1500 °C – 10 h	738 ± 254	314 ± 108	85 ± 42	58 ± 29	62 ± 26

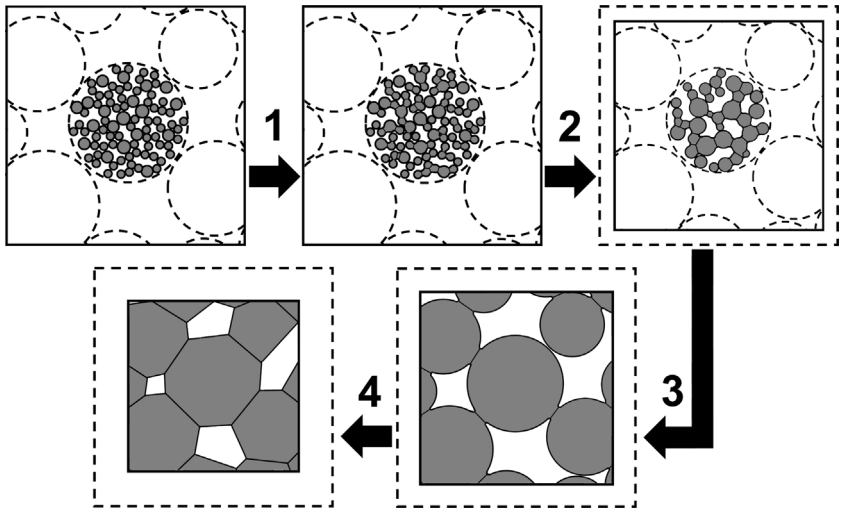

Fig. 4. Phenomenological 4 stage model illustrating the phases of sintering of an agglomerated nanomaterial. For the model description please refer to the text.

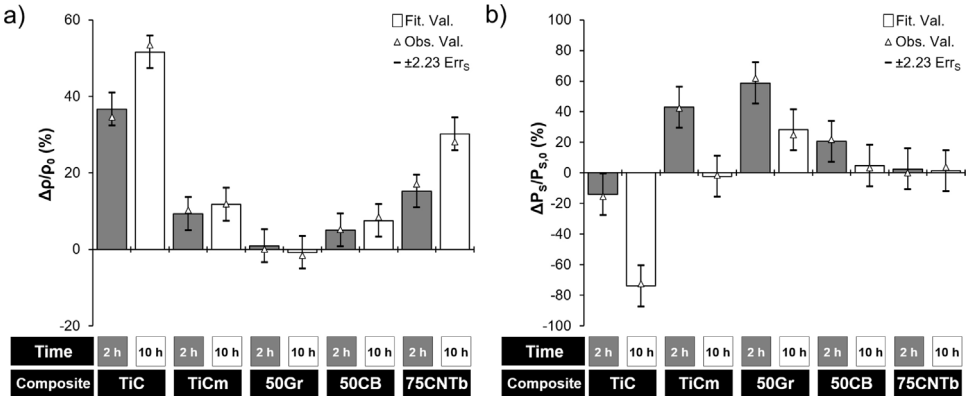

Fig. 5. TiC, TiCm, 50Gr, 50CB and 75CNTb $\Delta\rho/\rho_0$ (a) and $\Delta P_S/P_{S,0}$ (b) for heat treatments at 1500 °C for 2 and 10 h. The error bars correspond to the standard error of the mean (Err$_S$) – 95% confidence intervals – for the adjusted values (columns) obtained by ANOVA – analysis of variance.

2. after neck formation the agglomerated particles start to grow, increasing the intra-agglomerate pore size (P_S) while $P_{r,<200\,nm}/P_{r,>200\,nm}$ decreases with densification (ρ_r increase);
3. the agglomerated grains continue to grow (with densification), increasing the overall average pore size (bringing to zero $P_{r,<200\,nm}$ and reducing P_S - since the pores can not be detected anymore by nitrogen adsorption - BJH model [42]), eventually sintering to a particle of approximately the same size of the original agglomerate;
4. the densification will then proceed among the densified agglomerates, slowly reducing $P_{r,>200\,nm}$ until ρ_r eventually reaches 1; in this phase sintering will likely proceed at a slow rate due to

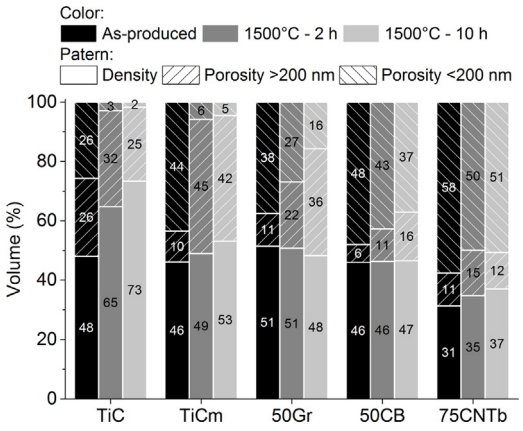

Fig. 6. Relative density and porosity ratios (below and above 200 nm) for the TiC, TiCm, 50Gr, 50CB and 75CNTb as-produced and heat treated for 2 and 10 h.

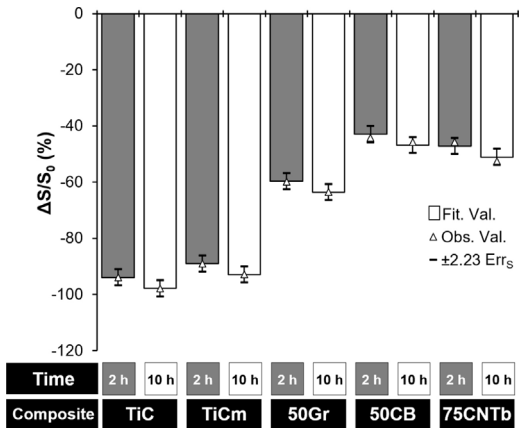

Fig. 7. TiC, TiCm, 50Gr, 50CB and 75CNTb $\Delta S/S_0$ for heat treatments at 1500 °C for 2 and 10 h. The error bars correspond to the standard error of the mean (Err_S) – 95% confidence intervals – for the adjusted values (columns) obtained by ANOVA – analysis of variance.

the stabilization of the structure by the existence of large pores which are difficult to eliminate.

The control charts of Figs. 5a, b and 7 were built using analysis of variance (ANOVA) in order to assess statistical significant differences of $\Delta\rho/\rho_0$, $\Delta P_S/P_{S,0}$ and $\Delta S/S_0$, respectively, for TiC, TiCm, 50Gr, 50CB and 75CNTb during heat treatments at 1500 °C for 2 and 10 h. In this figure the average values (triangle), the adjusted values from ANOVA (column) and respective 95% confidence intervals (column error bars) are represented. To complement the control charts, the obtained ρ_r and porosity, P_r, can be found represented in Fig. 6, where P_r is divided accordingly to porosity below ($P_{r,<200\,nm}$) and above 200 nm ($P_{r,>200\,nm}$). The absolute values for all the sintering parameters studied (ρ, SSA, P_S, $v_{P,BJH}$, $\Delta m/m_0$ and G_{SEM}) can be found in Table 2.

3.2.1. Titanium carbide sintering behaviour

Milled and non-milled TiC was subjected to the same heat treatments as the produced nanocomposites to serve as control samples. A TiC sample was milled for 2 h (named TiCm), heat treated at 1500 °C for 10 h, together with a non-milled sample where the milling was seen to hinder the TiC sintering even with no carbon addition. The microstructures resulting from the heat treatments can be seen in Fig. 8a for TiC and Fig. 8b for TiCm. TiC has a G_{SEM} of about 738 ± 254 nm and TiCm around 314 ± 108 nm which are close to their $D_{v,50}$ values as measured by laser scattering: 1.70 μm for TiC and 0.37 μm for TiC milled for 2 h (Fig. 2a – milling times of 0 h and 2 h). This result seems to already point that for both cases at 10 h we are on the stage 4 of the proposed model, where the primary particles in the agglomerates sinter and only after this do the dense agglomerates sinter among themselves.

The large SSA losses seen for both TiC and TiCm, can likely be related to the stage 1 of the sintering model, as expected for nanomaterials, bringing not so large densifications, as seen in, for example, TiCm for 2 h: large losses of SSA with relatively low changes in density (Figs. 7 and 5a). Stage 2, characterized by the decrease of $P_{r,<200\,nm}$ (Fig. 6) and increase in P_S (Fig. 5a), is seen for TiCm at 2 h. Alternatively this latter value can also be influenced by the smaller inter-agglomerate pores of TiCm (smaller agglomerates), which can be below 200 nm and thus be detected by BJH. At 10 h this is followed by the end of stage 3 at 10 h, where the P_S decreases again and the agglomerates densify (as seen before).

In the TiCm case, we seem to be in the presence of differential sintering where the agglomerates shrink more than the full body. This is seen from the reduction of $P_{r,<200\,nm}$, in Fig. 6 – agglomerate sintering – where it should cause a large densification where instead it converts into $P_{r,>200\,nm}$ without much densification. Probably, due to the much larger agglomerate size and smaller $P_{r,<200\,nm}/P_{r,>200\,nm}$ ratio initially in the TiC compared to TiCm, the shrinking of the agglomerates during sintering dominates the shrinking of the compact. This leads to an overall larger ρ_r for TiC than TiCm (ρ_r = 73% for TiC and 53% for TiCm for 10 h at 1500 °C).

Although in the literature reduction of the agglomerate size of nanometric powders is known to increase their densification (and so sintering kinetics) [17,15], such is not seen in the data presented here. Nevertheless, sintering is not complete in either case, so if higher temperatures would be used, TiCm should reach faster full density, due to the smaller agglomerate sizes. However, if the introduction of Zr in the case of TiCm, acts as a dopant that hinders the sintering, this could help explain the obtained lower densities, but no studies on Zr doped TiC could be found in the literature.

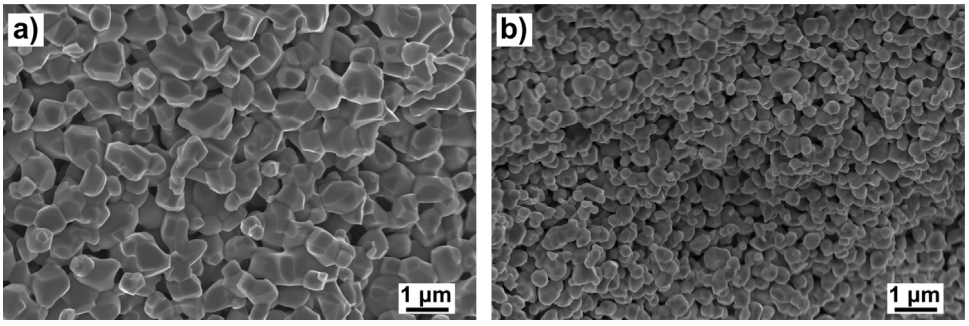

Fig. 8. SEM microstructures of TiC heat treated at 1500 °C for 10 h (a) and of TiC milled, TiCm, for 2 h and with the same heat treatment (b). G_{SEM} is 738 ± 254 nm for TiC and 314 ± 108 nm for TiCm.

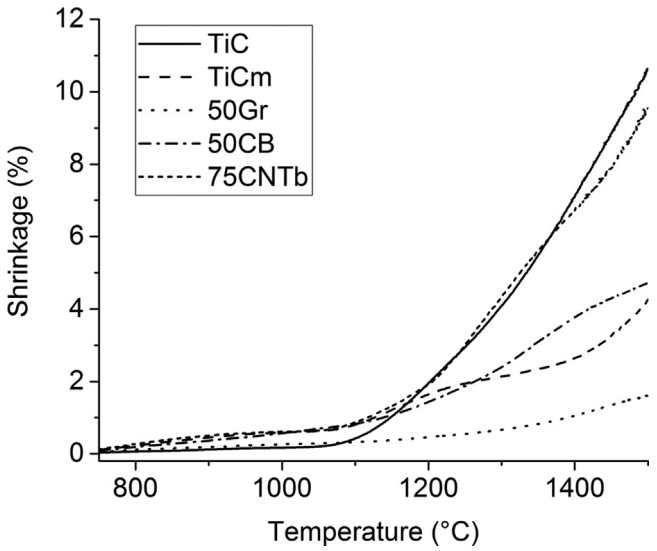

Fig. 9. Dilatometry of TiC, TiCm, 50Gr, 50CB and 75CNTb up to 1500 °C.

In the intermediate stages, the network of large pores (once inter-agglomerate pores) could hinder the sintering as soon as they are formed, which happens sooner for TiCm than TiC, thus explaining the results obtained.

Complementarily, in the dilatometry represented in Fig. 9 both TiC and TiCm seem to start sintering at the same temperatures, of about 1100 °C, although they reach different shrinkages. Furthermore, TiC sinters continuously with no rate decrease while TiCm shows some shrinkage before 1100 °C and rate changes around 1200 and 1400 °C which is likely due to mass losses due to the presence of ZrO_2 milling contaminants [46].

3.2.2. TiC-graphite composites

The 50 vol.% graphite-TiC composite (50Gr) SEM microstructures, as-produced and heat treated at 1500 °C for 10 h, can be seen in Fig. 10a and b respectively. Comparing these microstructures, it can be seen that the TiC has grown in particle size, but is not even near to the TiC or TiCm cases (Figs. 8a and b). Furthermore, G_{SEM} was determined to be 85 ± 42 nm, which is much smaller than the TiC cases. Consequently, just from the SEM microstructures it is clear that TiC sintering is hindered to a large extent by the presence of graphite.

Since the graphite SSA is small when compared to TiC (Table 1) and graphite particle sizes are not drastically affected during milling, the main contribution to the SSA of 50Gr comes from the TiC. When heat treating the 50Gr, the $\Delta S/S_0$ values for 2 and 10 h in Fig. 7, are both around −60%. This SSA reduction can only be due to the TiC sintering, since graphite particles are not expected to sinter. Although reduced, the percolation of the TiC particles in 50Gr still exists in between the graphite particles, as can be seen in the SEM microstructure of Fig. 10a. As a result TiC–TiC contacts will have a constrained sintering, which results in a reduced and stable over time $\Delta S/S_0$ when comparing with TiC or TiCm. In the same composite, the almost negligible $\Delta\rho/\rho_0$ (Fig. 5a) and shrinkage (Fig. 9) are due to the size of the graphite particles which are around 2 orders of magnitude larger than the TiC, creating a very stable, non-sinterable skeleton for the microstructure.

The $P_{r,>200\,nm}$ of 50Gr before heat treatment is low (Fig. 6) which shows that the mixing was quite successful since there is a good filling of TiC in the big pores created by the graphite micrometric particles. Otherwise, one would expect a large $P_{r,>200\,nm}$ from the graphite micrometric size. Even though $\Delta S/S_0$ values don't change much, from 2 to 10 h (Fig. 7), the $P_{r,<200\,nm}/P_{r,>200\,nm}$ is reducing for these times, showing that sintering still exists where the TiC particles percolate.

The $\Delta P_S/P_{S,0}$ values in Fig. 5b is positive for 2 h, indicating that stage 2 of the proposed model is on-going and stage 3 is starting for the 10 h value, due to the reduction of both $\Delta P_S/P_{S,0}$ and $P_{r,<200\,nm}$.

3.2.3. TiC-carbon black composites

Fig. 10b and d shows respectively the microstructures of the 50CB before and after heat treatment at 1500 °C – 10 h, where barely any change in particle sizes is seen. This shows that CB is very effective hindering the sintering of TiC. Due to their similar size and when homogeneously mixed, CB reduces the TiC coordination number significantly which hinders its sintering. In these microstructures, the CB is not easily distinguished from the TiC particles, but it was still possible to determine the G_{SEM} for 10 h of sintering – showing 58 ± 29 nm.

Due to the CB effect and its nanometric nature, high $P_{r,<200\,nm}$ values on the 50CB are kept after the 1500 °C heat treatments, as seen in Fig. 6, where the P_S is not changing much with the heat treatments (Fig. 5b). For the 50CB composites it is likely that phase 1 of the proposed model has just passed, where neck formation happened where possible and particle growth is hindered by the CB and sintering stagnates at phase 2.

50CB presents the lowest $\Delta S/S_0$ – a very sensitive parameter to the sintering of TiC - of all composites (Fig. 7). It also presents very stable ρ_r values in Fig. 6 and small $\Delta\rho/\rho_0$ in Fig. 5a. Curiously, the dilatometry of 50CB in Fig. 9 shows small shrinkages close to the values of TiCm. Both, at around 1400 °C, present changes in the shrinkage rate: in the case of TiCm the shrinkage rate is increasing while for 50CB it is decreasing (effect of the carbon black addition).

3.2.4. TiC-MWCNT composites

From the MWCNT composites, only 75CNTb will be discussed here, where in the others the milling had a detrimental effect on the MWCNT, as was discussed in Section 3.1. Further results on the 25, 50 and 75CNT can be found in the supplementary materials A.1.2.

When comparing the $\Delta\rho/\rho_0$ of 75CNTb in Fig. 5 with the other nanocomposites it is noticeable that 75CNTb presents the highest density variation, up to 28%. Although these $\Delta\rho/\rho_0$ are high, they are likely related with the relatively high mass losses of 75CNTb (Table 2) which can easily collapse the very porous structure of the composite (ρ_r = 31% for 75CNTb, Fig. 6). Although these density differences are quite high in absolute terms (Fig. 5a), ρ_r values at 10 h of heat treatment are still the lowest of all the composites (37% at 10 h). In the dilatometry of 75CNTb in Fig. 9 its shrinkage is as high as TiC, which is not due to TiC sintering but the mass losses.

Even though there are large $\Delta\rho/\rho_0$ values, looking at the microstructures of 75CNTb before and after 1500 °C – 10 h (Figs. 3c and d, respectively) there is barely any sintering happening, were TiC sizes at 10 h are $G_{SEM} = 62 \pm 26$ nm (Table 2). Furthermore, the pore structure of the 75CNTb is dominated by $P_{r,<200\,nm}$ in all stages where very small $\Delta P_S/P_{S,0}$ values (Fig. 5b) are verified as well, where both come from the MWCNT effect on the microstructure.

Relatively to the SSA, the 75CNTb composites have the highest absolute values both before and after heat treatments, 49.8 $m^2\,g^{-1}$ before and 23.6 $m^2\,g^{-1}$ after – Table 2, with similar $\Delta S/S_0$ to 50CB (Fig. 7).

It is relevant to mention that in the case of the MWCNT composites, for the volume calculations the bulk density of MWCNT was used (Table 1), which is much smaller than graphite and carbon black densities. If calculated in mass, the 50Gr and 50CB, the carbon percentages initially added are were around 30 wt.%, while for 75CNTb it was only 8.4 wt.%. Thus, with small quantities of MWCNT

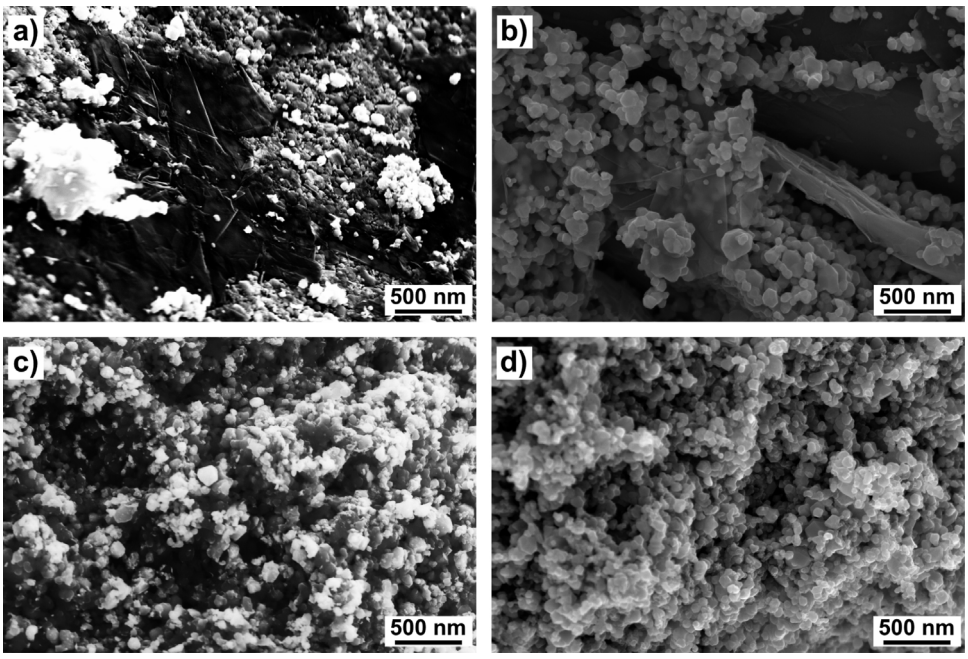

Fig. 10. SEM microstructures of 50Gr before (a) and after (b) heat treatment at 1500 °C for 10 h and of 50CB before (c) and after (d) the same heat treatment. For 50Gr and 50CB after 1500 °C – 10 h, G_{SEM} is 85 ± 42 nm and 58 ± 29 nm, respectively.

(when not co-milled), the sintering of TiC is very efficiently hindered.

4. Conclusions

Even though TiC-C composites are present in the literature, their characteristics are not suited for the application as ISOL target materials for the production of isotopes by high energy particle bombardment. A new processing route had to be developed in order to stabilize nanometric TiC under high temperatures.

TiC as supplied (48 nm) sinters at 1500 °C to grain sizes of 738 ± 254 nm. When milled for 2 h TiC sintering was hindered, where at 1500 °C the TiC the grain sizes were about 314 ± 108 nm. In any case, even with the latter result (milling TiC) nanometric TiC could not be maintained at 1500 °C, so carbon addition was investigated to maintain a nanometric structure at high temperatures.

A successful processing route was created to produce three different TiC – Carbon nanocomposites: TiC – Carbon Black, TiC – Graphite and TiC – multi wall carbon nanotubes (MWCNT). Attrition milling was used to co-mill the nanocomposites in isopropanol, except for the TiC-MWCNT composite where MWCNT were added later to the TiC, to avoid destruction of the MWCNT. The obtained composites were heat treated at 1500 °C for 2 and 10 h to assess TiC sintering hindering.

All 3 different carbon allotropes used, successfully hindered the sintering of nanometric TiC where the best stability was in the TiC-MWCNT, followed by TiC-carbon black and finally TiC-graphite. At 1500 °C for 10 h TiC-MWCNT showed TiC particles of 62 ± 26 nm, and 37% density, with only 8.4 wt.% C addition to TiC. Where in the others, with around 30 wt.% of C addition to TiC, after the same heat treatment conditions, grain sizes of 58 ± 29 nm and 85 ± 42 nm with densities around 50% were obtained for TiC-carbon black and TiC-graphite composites, respectively.

In the current tests we aimed for stability of nanometric TiC at 1500 °C. Since for the application in sight can benefit from higher temperatures (such as 1800 °C) to bring faster isotope releases, these nanocomposites were tested at higher temperatures and presented in another publication [46]. Furthermore, the zirconium oxide and consequent carbide formation, with the respective mass losses need to be studied in detail to ascertain its impact on the nanocomposites and phase stability, a key factor for production of stable and high intensity radioactive ion beams in practice.

Acknowledgments

The authors would like to acknowledge Carlos Morais for the technical expertise with the attrition milling, Filipe Oliveira, for lending the dilatometer equipment and Prof. Jacques Lemaître for the ANOVA – analysis of variance – calculation tools and interesting discussions. We would like to acknowledge as well Orion Engineered Carbons, S.A. for supplying the carbon black for this study as well as CERN and EPFL for funding this research project.

Appendix A. Supplementary data

Supplementary data associated with this article can be found, in the online version, at http://dx.doi.org/10.1016/j.jeurceramsoc.2017.04.016.

References

[1] T.Y. Kosolapova, Carbides – Properties, Production and applications, Plenum Press, New York/London, 1971.
[2] H.O. Pierson, Handbook of Refractory Carbides and Nitrides: Properties, Characteristics, Processing, and Applications, Noyes Publications, Bracknell, 1996.
[3] A. Mullendore, J. Whitley, D. Mattox, The development and laboratory testing of low refractory coatings for fusion reactor limiters, J. Nucl. Mater. 93-94 (9) (1980) 486–492, http://dx.doi.org/10.1016/0022-3115(80)90162-2.
[4] J.M. Ramos-Fernández, M. Martínez-Escandell, F. Rodríguez-Reinoso, Production of nanoTiC-graphite composites using Ti-doped self-sintering carbon mesophase powder, J. Eur. Ceram. Soc. 33 (3) (2013) 583–591, http://dx.doi.org/10.1016/j.jeurceramsoc.2012.09.019.
[5] C. Dickerson, Y. Yang, T.R. Allen, Defects and microstructural evolution of proton irradiated titanium carbide, J. Nucl. Mater. 424 (1-3) (2012) 62–68, http://dx.doi.org/10.1016/j.jnucmat.2012.02.005.
[6] E. Kugler, The ISOLDE facility, Hyperfine Interact. 129 (2000) 23–42, http://dx.doi.org/10.1023/A:1012603025802.
[7] L. Carraz, I. Haldorsen, H. Ravn, M. Skarestad, L. Westgaard, Fast release of nuclear reaction products from refractory matrices, Nucl. Instrum. Methods 148 (2) (1978) 217–230, http://dx.doi.org/10.1016/0029-554X(70)90171-0.

[8] P. Hoff, O. Jonsson, E. Kugler, H. Ravn, Release of nuclear reaction products from refractory compounds, Nucl. Instrum. Methods Phys. Res. 221 (2) (1984) 313–329, http://dx.doi.org/10.1016/0167-5087(84)90002-4.

[9] U. Köster, Intense radioactive-ion beams produced with the ISOL method, Eur. Phys. J. A – Hadrons Nuclei 15 (1-2) (2002) 255–263, http://dx.doi.org/10.1140/epja/i2001-10264-2.

[10] A. Gottberg, Target materials for exotic ISOL beams, Nucl. Instrum. Methods Phys. Res. Sect. B: Beam Interact. Mater. Atoms (2017), http://dx.doi.org/10.1016/j.nimb.01.2016020.

[11] S. Fernandes, Submicro- and Nano-Structured Porous Materials for Production of High-Intensity Exotic Radioactive Ion Beams, École polytechnique fédérale de Lausanne, 2010, http://dx.doi.org/10.5075/epfl-thesis-4813 (Phd thesis).

[12] T. Stora, Recent developments of target and ion sources to produce ISOL beams, Nucl. Instrum. Methods Phys. Res. Sect. B: Beam Interact. Mater. Atoms 317 (PART B) (2013) 402–410, http://dx.doi.org/10.1016/j.nimb.2013.07.024.

[13] J.P. Ramos, A. Gottberg, R. Augusto, T. Mendonca, K. Riisager, C. Seiffert, P. Bowen, A. Senos, T. Stora, Target nanomaterials at CERN-ISOLDE: synthesis and release data, Nucl. Instrum. Methods Phys. Res. Sect. B: Beam Interact. Mater. Atoms 376 (2016) 81–85, http://dx.doi.org/10.1016/j.nimb.2016.03.003.

[14] J.P. Ramos, A. Gottberg, T. Mendonça, C. Seiffert, A. Senos, H. Fynbo, O. Tengblad, J. Briz, M. Lund, G. Koldste, M. Carmona-Gallardo, V. Pesudo, T. Stora, Intense $^{31-35}$Ar beams produced with a nanostructured CaO target at ISOLDE, Nucl. Instrum. Methods Phys. Res. Sect. B: Beam Interact. Mater. Atoms 320 (2014) 83–88, http://dx.doi.org/10.1016/j.nimb.2013.12.009.

[15] Nanostructured Materials: Processing, Properties and Potential Applications, in: C.C. Koch (Ed.), 2nd ed., Noyes Publications, New York, 2002.

[16] S. Panfilov, O. Padalko, N. Mitrenko, Behavior of ultrafine titanium carbide powders during annealing and sintering, Soviet Powder Metal. Metal Ceram. 24 (11) (1985) 824–828, http://dx.doi.org/10.1007/BF00802551.

[17] P. Bowen, C. Carry, From powders to sintered pieces: forming, transformations and sintering of nanostructured ceramic oxides, Powder Technol. 128 (2-3) (2002) 248–255, http://dx.doi.org/10.1016/S0032-5910(02)00183-3.

[18] L.C.D. Jonghe, M.N. Rahaman, Sintering of ceramics, in: S. Somiya, F. Aldinger, N. Claussen, R.M. Spriggs, K. Uchino, K. Koumoto, M. Kaneno (Eds.), Handbook of Advanced Ceramics, Volume I: Materials Science, Elsevier, Academic Press, 2003, pp. 187–264, http://dx.doi.org/10.1016/B978-012654640-8/50006-7, Chapter 4.

[19] J.D. French, M.P. Harmer, H.M. Chan, G.A. Miller, Coarsening-resistant dual-phase interprenetrating microstructures, J. Am. Ceram. Soc. 73 (8) (1990) 2508–2510, http://dx.doi.org/10.1111/j.1151-2916.1990.tb07621.x.

[20] M.W. Weiser, L.C. De Jonghe, Inclusion size and sintering of composite powders, J. Am. Ceram. Soc. 71 (3) (1988) C-125–C-127, http://dx.doi.org/10.1111/j.1151-2916.1988.tb05030.x.

[21] L. Olmos, C.L. Martin, D. Bouvard, Sintering of mixtures of powders: experiments and modelling, Powder Technol. 190 (1–2) (2009) 134–140, http://dx.doi.org/10.1016/j.powtec.2008.04.057.

[22] B. Manley, J.B. Holt, Z.A. Munir, Sintering of combustion-synthesized titanium carbide, in: Materials Science Research, Springer US, Boston, MA, 1984, pp. 303–316, http://dx.doi.org/10.1007/978-1-4613-2761-5_22.

[23] L. Stobierski, A. Gubernat, Sintering of silicon carbide I. Effect of carbon, Ceram. Int. 29 (3) (2003) 287–292, http://dx.doi.org/10.1016/S0272-8842(02)00117-7.

[24] D. Cho, J. Hoon Park, Y. Jeong, Y. Lak Joo, Synthesis of titanium carbide–carbon nanofibers via carbothermal reduction of Titania with carbon, Ceram. Int. 41 (9) (2014) 10974–10979, http://dx.doi.org/10.1016/j.ceramint.2015.05.041.

[25] K. Thorne, S.J. Ting, C.J. Chu, J.D. Mackenzie, T.D. Getman, M.F. Hawthorne, Synthesis of TiC via polymeric titanates: the preparation of fibres and thin films, J. Mater. Sci. 27 (16) (1992) 4406–4414, http://dx.doi.org/10.1007/BF00541573.

[26] J.R. Martin, L. Borchardt, M. Oschatz, G. Mondin, S. Kaskel, Titanium carbide and carbide-derived carbon composite nanofibers by electrospinning of Ti-resin precursor, Chemie-Ingenieur-Technik 85 (11) (2013) 1742–1748, http://dx.doi.org/10.1002/cite.201300057.

[27] Y. Zhao, A. Thapa, Q. Feng, M. Xi, Q. Qiao, H. Fong, Electrospun TiC/C nano-felt surface-decorated with Pt nanoparticles as highly efficient and cost-effective counter electrode for dye-sensitized solar cells, Nanoscale 5 (23) (2013) 11742–11747, http://dx.doi.org/10.1039/c3nr04170k.

[28] G. Zhou, T. Xiong, S. Jiang, S. Jian, Z. Zhou, H. Hou, Flexible titanium carbide–carbon nanofibers with high modulus and high conductivity by electrospinning, Mater. Lett. 165 (2016) 91–94, http://dx.doi.org/10.1016/j.matlet.2015.11.119.

[29] T. Yu, Y. Deng, L. Wang, R. Liu, L. Zhang, B. Tu, D. Zhao, Ordered mesoporous nanocrystalline titanium-carbide/carbon composites from in situ carbothermal reduction, Adv. Mater. 19 (17) (2007) 2301–2306, http://dx.doi.org/10.1002/adma.200700667.

[30] Z. Abdullaeva, E. Omurzak, C. Iwamoto, H. Okudera, M. Koinuma, S. Takebe, S. Sulaimankulova, T. Mashimo, High temperature stable WC_{1-x}@C and TiC@C core–shell nanoparticles by pulsed plasma in liquid, RSC Adv. 3 (2) (2013) 513, http://dx.doi.org/10.1039/c2ra22028h.

[31] V. Kiran, K.L. Nagashree, S. Sampath, Synergistic electrochemical activity of titanium carbide and carbon towards fuel cell reactions, RSC Adv. 4 (24) (2014) 12057–12064, http://dx.doi.org/10.1039/c3ra46281a.

[32] J.L. Li, L.J. Wang, G.Z. Bai, W. Jiang, Microstructure and mechanical properties of in situ produced TiC/C nanocomposite by spark plasma sintering, Scr. Mater. 52 (9) (2005) 867–871, http://dx.doi.org/10.1016/j.scriptamat.2005.01.006.

[33] W. Yang, L. Zhang, Y. Liu, L. Cheng, W. Zhang, Preparation and mechanical properties of carbon fiber reinforced $(BC_x–SiC)_n$ multilayered matrix composites, Appl. Compos. Mater. 14 (4) (2007) 277–286, http://dx.doi.org/10.1007/s10443-007-9046-y.

[34] I.L. Shabalin, D.M. Tomkinson, L.I. Shabalin, High-temperature hot-pressing of titanium carbide-graphite hetero-modulus ceramics, J. Eur. Ceram. Soc. 27 (5) (2007) 2171–2181, http://dx.doi.org/10.1016/j.jeurceramsoc.2006.07.008.

[35] X. Wang, M. Lu, L. Qiu, H. Huang, D. Li, H. Wang, Y.B. Cheng, Graphene/titanium carbide composites prepared by sol–gel infiltration and spark plasma sintering, Ceram. Int. 42 (1) (2015) 122–131, http://dx.doi.org/10.1016/j.ceramint.2015.08.017.

[36] P. Bowen, R. Mulone, P. Streit, T.A. Ring, Slip Casting of TiC_xN_{1-x} – Mo_2C-Ni Cermets, in: P. Duran, J. Fernandez (Eds.), Third Euro-Ceramics – Volume 1, Faenza Editrice Iberica, 1993, pp. 549–554.

[37] D.R. Lide (Ed.), CRC Handbook of Chemistry and Physics, 90th ed., CRC Press, 2010.

[38] R.M. German, A measure of the number of particles in agglomerates, Int. J. Powder Metal. 32 (4) (1996) 365–373.

[39] E.D. Palik (Ed.), Handbook of Optical Constants of Solids, Elsevier, 1998.

[40] J. Janzen, The refractive index of colloidal carbon, J. Colloid Interface Sci. 69 (3) (1979) 436–447, http://dx.doi.org/10.1016/0021-9797(79)90133-4.

[41] S. Brunauer, P. Emmett, E. Teller, Adsorption of gases in multimolecular layers, J. Am. Chem. Soc. 60 (2) (1938) 309–319, http://dx.doi.org/10.1021/ja01269a023.

[42] E.P. Barrett, L.G. Joyner, P.P. Halenda, The determination of pore volume and area distributions in porous substances. I. Computations from nitrogen isotherms, J. Am. Chem. Soc. 73 (1) (1951) 373–380, http://dx.doi.org/10.1021/ja01145a126.

[43] C.A. Schneider, W.S. Rasband, K.W. Eliceiri, NIH image to ImageJ: 25 years of image analysis, Nat. Methods 9 (7) (2012) 671–675, http://dx.doi.org/10.1038/nmeth.2089.

[44] D.C. Montgomery, Design and Analysis of Experiments, 8th ed., John Wiley & Sons, Inc., 2012.

[45] B. Munkhbayar, M.J. Nine, J. Jeoun, M. Bat-Erdene, H. Chung, H. Jeong, Influence of dry and wet ball milling on dispersion characteristics of the multi-walled carbon nanotubes in aqueous solution with and without surfactant, Powder Technol. 234 (2013) 132–140, http://dx.doi.org/10.1016/j.powtec.2012.09.045.

[46] J.P. Ramos, Titanium Carbide–Carbon Porous Nanocomposite Materials for Radioactive Ion Beam Production: Processing, Sintering and Isotope Release Properties (PhD thesis), École polytechnique fédérale de Lausanne (EPFL), 2017, http://dx.doi.org/10.5075/epfl-thesis-7363, CERN-THESIS-2016-247 https://cds.cern.ch/record/2243566?ln=en.

[47] J.P. Ramos, C. Fernandes, T. Stora, A. Senos, Sintering kinetics of nanometric calcium oxide in vacuum atmosphere, Ceram. Int. 41 (6) (2015) 8093–8099, http://dx.doi.org/10.1016/j.ceramint.2015.03.007.

[48] A. Senos, J. Vieira, Processing effects on morphological evolution of ZnO during sintering, in: P. Vincenzini (Ed.), Proceedings of the World Ceramics Congress, part of the 6th CIMTEC, Advances in Science and Technology, 3C, Ceramics – Charting the Future, Techna Srl, Florence, Italy, 1995, pp. 1777–1784.